Competing Jahn-Teller distortions and hydrostatic pressure effects in the quasi-one-dimensional quantum ferromagnet $CuAs_2O_4$

K. Caslin,[1,2,*] R. K. Kremer,[1] F. S. Razavi,[2] M. Hanfland,[3] K. Syassen,[1] E. E. Gordon,[4] and M.-H. Whangbo[4]

[1]*Max-Planck-Institut für Festkörperforschung, Heisenbergstrasse 1, D-70569 Stuttgart, Germany*

[2]*Brock University, 500 Glenridge Avenue, Saint Catharines, Ontario, Canada L2S-3A1*

[3]*European Synchrotron Radiation Facility, 6 Rue Jules Horowitz, 38000 Grenoble, France*

[4]*Department of Chemistry, North Carolina State University, Raleigh, North Carolina 27695-8204, USA*

(Received 10 June 2015; revised manuscript received 20 August 2015; published 7 January 2016; corrected 14 January 2016)

$CuAs_2O_4$ is a $S = 1/2$ quasi-one-dimensional ribbon chain compound which orders ferromagnetically at 7.4 K under ambient conditions. $CuAs_2O_4$ features nearest- and next-nearest-neighbor spin-exchange interactions along the spin chains with a ratio $\alpha = J_{nn}/J_{nnn}$ in close proximity to the quantum critical point at $\alpha = -4$. We apply hydrostatic pressure up to ~11.5 GPa and examine the structural and magnetic properties using Raman spectroscopy, single-crystal synchrotron x-ray diffraction, and magnetic susceptibility measurements. External pressure severely reduces the axial Jahn-Teller elongations of the oxygen octahedra surrounding the Cu^{2+} cations and stabilizes the ferromagnetic ground state. At 9.2(2) GPa, we detect a structural phase transition leading to an increased twisting of the CuO_2 ribbon chains and a large drop of the magnetic ordering temperature. *Ab initio* density functional theory calculations of the spin-exchange parameters, using the structural parameters as a function of pressure, support the experimental findings.

DOI: 10.1103/PhysRevB.93.022301

I. INTRODUCTION

The magnetic properties of antiferromagnetic (AFM) quantum spin chains with competing nearest-neighbor (NN) and next-nearest-neighbor (NNN) spin-exchange interactions have attracted much attention since they may exhibit unusual magnetic ground states [1–7]. Of particular interest are systems that develop incommensurate helicoidal magnetic ordering which can induce multiferroic behavior [8–10]. This has been observed in a number of compounds containing $Cu^{2+}X_2$ ribbon chains. Such ribbon chains with $X = O^{2-}$ are found in the title compound, $CuAs_2O_4$, shown in Fig. 1. CuX_2 ribbon chains form when Jahn-Teller-distorted anion octahedra surrounding the Cu^{2+} cations ($3d^9$ electronic configuration with spin $S = 1/2$) are linked via opposite edges of their basal planes to form infinite aggregates [11]. In such ribbon chains, the NN spin-exchange interaction via a Cu–X–Cu bond with bonding angle close to 90° is small and typically ferromagnetic (FM); thus the NNN spin-exchange interaction via two intermediate anions may be the dominant spin-exchange interaction. A prominent example of such a ribbon chain system that exhibits a helicoidal multiferroic ground state is $LiCuVO_4$. The helicoidal ordering in $LiCuVO_4$ was shown with neutron-scattering experiments [1,3]. Multiferroicity was first reported by Naito *et al.* [9] and has been further investigated since [12–16]. Polarized neutron-scattering experiments have favorably been used to reveal the chirality of the spin helices which can be switched by magnetic and electric fields [17,18]. Other cuprates which display helicoidal order include $NaCu_2O_2$, Li_2CuO_2, and $PbCuSO_4(OH)_2$ [2,7,8,19–22]. Most of the ribbon chain systems identified so far contain O^{2-} anion octahedra surrounding the Cu^{2+} cations. Lately, we have demonstrated that the binary halide ribbon chain systems, $CuCl_2$ and $CuBr_2$, also show helicoidal antiferromagnetic order [23,24]. Both compounds have also been found to exhibit multiferroic behavior, $CuBr_2$ with a notably high transition temperature of ~74 K [25,26].

In CuO_2 ribbon chains, deviations from the Heisenberg spin-exchange coupling due to spin-orbit effects become important. The deviations often introduce a slight easy-plane anisotropy [27] which forces the Cu^{2+} moments to spiral in, or close to, the basal planes of the CuX_6 octahedra. Hikihara *et al.* [28], and later on Furukawa *et al.* [29], demonstrated that a small easy-plane anisotropy tends to stabilize the chiral order in ribbon chain systems with ferromagnetic NN spin-exchange interactions. However, in the case of large easy-plane anisotropy, chiral order is expected to be replaced by a dimer order [29]. For the case of antiferromagnetic NN spin-exchange interactions, a gapped singlet-dimer state is the expected ground state [29]. Of particular interest are systems with small easy-plane anisotropy that lay close to the classical chiral limit at $\alpha = J_{nn}/J_{nnn} = -4$. Increasing the NN ferromagnetic spin exchange in such compounds may move them from a dimer or chiral ground state, across a quantum critical point, to a ferromagnetic ground state [29].

So far, experimental realizations of systems close to the quantum critical limit at $\alpha = -4$ are rare. Drechsler *et al.* [5] and subsequently Schmitt *et al.* [30] investigated the compound Li_2ZrCuO_4 and deduced a ratio $\alpha = J_{nn}/J_{nnn} \approx -4.5$. They proposed Li_2ZrCuO_4 to be a "missing link" near the quantum critical point [5,30]. According to magnetic susceptibility studies, Li_2ZrCuO_4 exhibits a three-dimensional antiferromagnetic ground state. The authors attribute long-range ordering to sizable interchain interactions which may be especially relevant in the quantum critical regime [30]. A conclusive clarification of the antiferromagnetic structure of Li_2ZrCuO_4 is still pending. Another system close to quantum criticality is $Ca_2Y_2Cu_5O_{10}$, which features ferromagnetically aligned spins along the ribbon chains. By local spin-density approximation+U and generalized gradient approximation

*Corresponding author: caslin.kevin@gmail.com

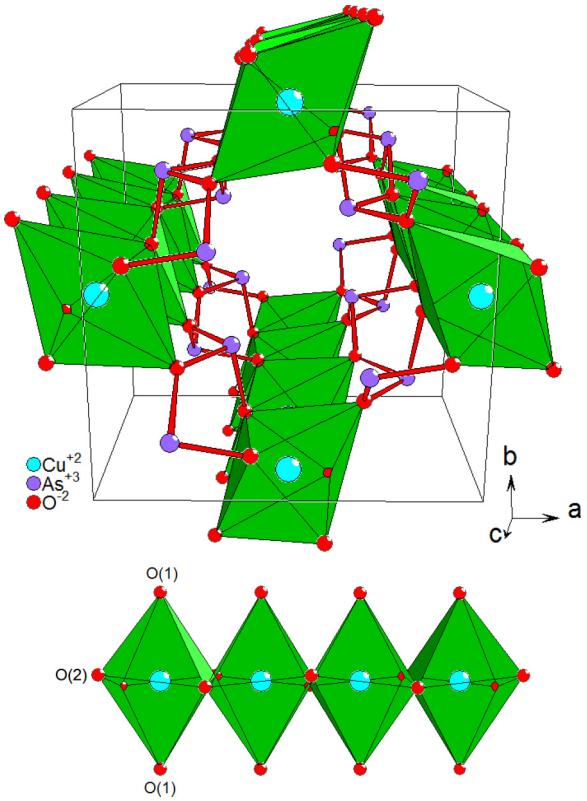

FIG. 1. The crystal structure of $CuAs_2O_4$ at ambient conditions and an isolated chain of CuO_6 octahedra. The CuO_2 ribbon chains are formed by linked Jahn-Teller distorted CuO_6 octahedra which run along the c axis. The apex O(1) and basal O(2) atoms are labeled.

(GGA)+U calculations, the ratio α was determined to be $\alpha \approx -5.3$, below the quantum critical point [31]. Similar to Li_2ZrCuO_4, $Ca_2Y_2Cu_5O_{10}$ was found to order antiferromagnetically below ∼29 K [32].

Recently, we reported the magnetic and thermal properties of $CuAs_2O_4$, the natural mineral Trippkeite [33]. GGA+U and transfer-matrix density-matrix renormalization-group calculations revealed a ratio $\alpha \sim -4.1$, indicating $CuAs_2O_4$ to lie closest to the quantum critical point, $\alpha = -4$, of all systems reported so far [33]. $CuAs_2O_4$ consists of slightly twisted CuO_2 ribbon chains (see Fig. 1) and orders ferromagnetically below a Curie temperature of $T_c = 7.6 \pm 0.2$ K. Single-crystal magnetization measurements showed a saturated Cu moment close to 1 μ_B already in magnetic fields above ∼1 T with the moment aligned in the a-b plane. First measurements of the Curie temperature under hydrostatic pressure up to ∼1.5 GPa resulted in a sizable increase of T_c by ∼1.4K/GPa indicating a stabilization of the ferromagnetic ground state with external pressure.

In this work, we have extended our investigations under hydrostatic pressures up to ∼11.5 GPa in order to establish the relationship between the structural and magnetic properties of $CuAs_2O_4$ [34]. We were particularly interested in whether the pressure-induced changes in the interatomic distances and angles could be used to tune the ratio of the NN and NNN spin-exchange interactions and possibly push $CuAs_2O_4$ towards a new magnetic ground state. We find that T_c of $CuAs_2O_4$ increases continuously with pressure up to ∼9 GPa where a structural phase transition occurs. Crystal-structure analysis with single-crystal x-ray-diffraction experiments up to ∼9 GPa indicates that the axial elongations of the CuO_6 octahedra caused by Jahn-Teller distortions were markedly suppressed. The derived structural parameters could favorably be used as input for *ab initio* calculations for the intrachain and interchain spin-exchange parameters versus pressure. Our density functional theory (DFT) GGA+U calculations indicate that external pressure up to ∼9 GPa increases the ferromagnetic NN spin exchange by about 40% whereas the antiferromagnetic NNN spin exchange remains approximately constant. The interchain spin-exchange parameters are more than an order of magnitude smaller than the intrachain exchange.

A single-crystal to single-crystal structural phase transition (phase I → phase II) was identified near ∼9 GPa by Raman spectroscopy and x-ray-diffraction measurements on single crystals. The crystal structure in phase II is characterized by an increased twisting of the CuO_2 ribbon chains and a tetragonal-to-orthorhombic distortion of the oxygen environment in the basal plane of the CuO_6 octahedra. The *ab initio* calculations indicated a further increase of the NN spin-exchange interaction and a nearly constant NNN spin-exchange interaction in phase II. Magnetic susceptibility measurements with pressure above 9 GPa identified a drastic reduction of the Curie temperature.

II. EXPERIMENTAL DETAILS

Small dark-green crystals of $CuAs_2O_4$, approximately 5×10^{-3} mm^3 in size, were prepared following the hydrothermal synthesis route described in detail by Pertlik [35]. Crystals that were well defined and homogeneous in color were selected for our studies.

Raman spectra were collected from single crystals loaded in a diamond anvil cell with a methanol-ethanol mixture as the pressure medium. The Raman spectrometer was a Jobin Yvon Typ V 010 LabRAM single grating system with a spectral resolution of ∼1 cm^{-1}. Linearly polarized He/Ne gas laser radiation of 632.8-nm wavelength was used. The power was kept to $\leqslant$1 mW to avoid heating the sample. Pressures were measured using the ruby R-line luminescence method [36].

High-pressure single-crystal x-ray-diffraction experiments were performed on the ID09A beamline at the European Synchrotron Radiation Facility. A monochromatic synchrotron x-ray beam with $\lambda = 0.413$ Å ($E \sim 30$ keV) focused to a spot size of 15×10 μm^2 was used. A membrane-driven high-pressure cell following a diamond anvil design with Boehler-Almax seats was employed providing an opening cone of 76°. The culet size was ∼600 μm and the crystallites were loaded together with He gas as the pressure transmitting medium. The stainless steel gasket with an initial hole diameter of 250 μm was preindented to a thickness of ∼80 μm [37]. Pressures were measured with the ruby fluorescence method using the calibration by Mao *et al.* [38]. Diffraction intensities were collected with a Mar555 flat-panel detector applying a ω rotation around a vertical-acting axis with an integrated step scan of 0.5° and a counting time of 1 s per frame. In

order to correct for variable diffracting volumes as a function of the ω position, frames were rescaled using the intensities of Friedel pairs. An absorption correction of the intensities was not found necessary due to the high energy of the x-ray beam. The collected diffraction data were processed and analyzed using CrysAlisPro-171.34.44, SIR2011, Crystals, and Jana2006 software packages [39–42].

Magnetic susceptibility measurements on small crystallites of $CuAs_2O_4$ were carried out in a Quantum Design magnetic property measurement system using a magnetic field of 0.01 T. A home-built CuBe pressure cell, following the design of Tateiwa *et al.* [43,44], equipped with nonmagnetic ceramic or diamond anvils and a 0.4-mm-thick CuBe gasket was employed. Degassed Glycerin or Daphne oil was used as the pressure transmitting medium. Pressures were determined from the superconducting transition temperature of high purity (99.9999%) Pb spheres also placed inside the pressure cell [45,46].

III. RESULTS AND DISCUSSION

A. Raman scattering

A detailed study of the Raman spectra of $CuAs_2O_4$ at ambient pressure has been previously carried out by Caslin *et al.* [33]. In order to search for pressure induced structural changes, the Raman spectra of $CuAs_2O_4$ single crystals were measured from 0 to 20 GPa at $T = 295$ K. The Raman spectra for various pressures are displayed in Fig. 2. With the limitations imposed by the diamond anvil cell, we can only identify five definite Raman modes out of the 26 expected from symmetry considerations [33]. At a pressure of 2.67 GPa, we find modes at wave numbers 203.5, 290.3, 382.3, 512.7, and 794 cm^{-1}, consistent with the previously published data for ambient pressure [33]. Up to 9 GPa, the Raman peaks shift to higher wave numbers reflecting the lattice stiffening due to external pressure. Above 9 GPa, new peaks and peak splittings appear and continue to grow as pressure is increased. These features indicate a structural phase transition at $\gtrsim$9 GPa. The Raman spectra of the high-pressure phase show an increased number of peaks compared to the ambient pressure phase, indicating a symmetry reduction of the crystal structure.

Figure 3 displays the Raman shift of the observed peaks versus the pressure and the unit-cell volume, $v(P)$, as determined from synchrotron x-ray diffraction (see below). It allows for the determination of the average Grüneisen parameters of the respective modes, γ_i, at the center of the Brillouin zone according to

$$\gamma_i = -\frac{\delta \ln[\omega_i(P)]}{\delta \ln[v(P)]} \approx -\frac{v(0)}{\omega_i(0)} \frac{\Delta\omega_i(P)}{\Delta v(P)}, \qquad (1)$$

where $\omega_i(P)$ is the frequency for the respective Raman mode, and $\Delta\omega_i(P)$ and $\Delta v(P)$ are the pressure induced changes in the frequency of the mode i and the pressure induced volume change, respectively.

For all Raman modes, a linear relationship $\Delta\omega_i(P)$ versus $\Delta v(P)$ can be fitted to the data. In Table I we have listed the initial linear slopes. A closer inspection of the E_g modes with resonance frequencies of 275.4 and 497.1 cm^{-1}, revealed slight deviations from linearity for pressures above ~7 GPa.

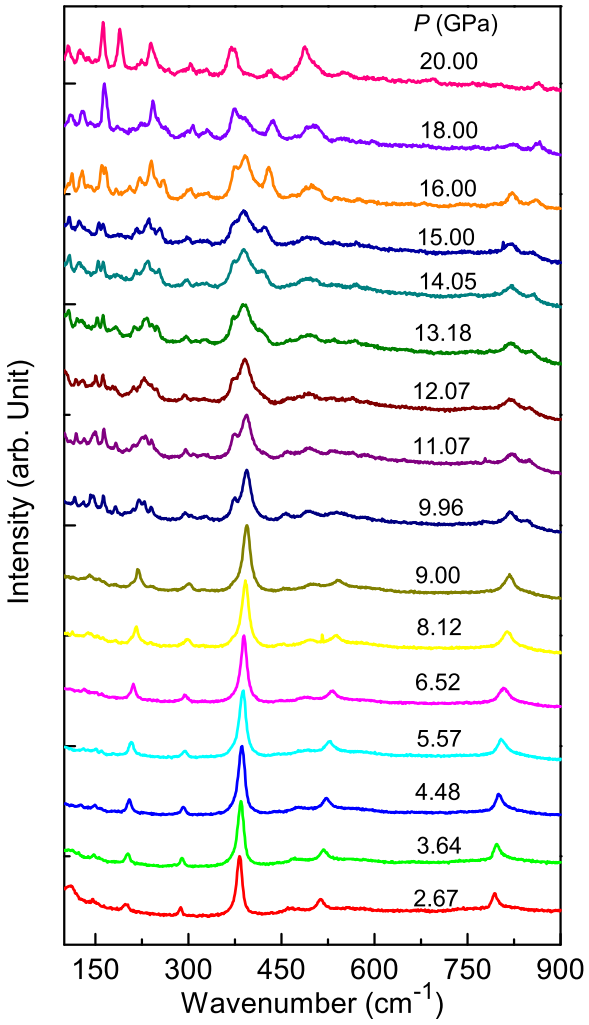

FIG. 2. Raman spectra of a single crystal of $CuAs_2O_4$ at various external pressures. Additional peaks appear above 9 GPa indicating the occurrence of a structural phase transition.

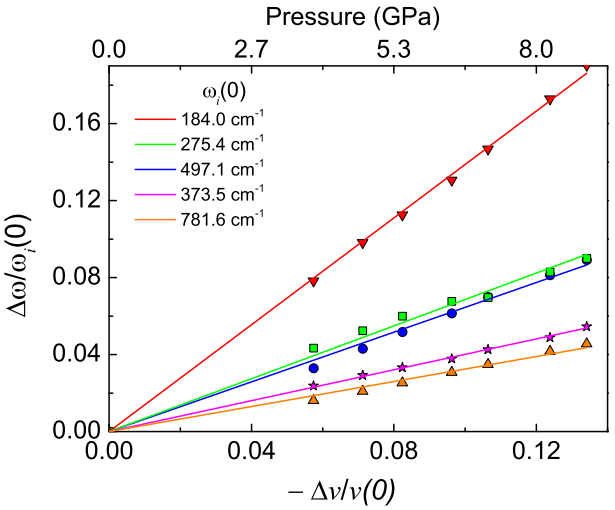

FIG. 3. Variation of the Raman resonance positions vs the unit-cell volume variation of $CuAs_2O_4$ in phase I. The solid lines represent linear slopes obtained from least-squares fits to Eq. (1).

TABLE I. Mode Grüneisen parameters, γ_i, for the five observed Raman modes obtained from the fits shown in Fig. 3. The $\omega_i(0)$ values are the ambient pressure frequencies for the selected Raman modes.

Symmetry	$\omega_i(0)$ (cm^{-1})	γ_i
E_g	184.0	1.39(1)
E_g	275.4	0.73(1)
E_g	373.5	0.40(1)
E_g	497.1	0.61(1)
B_{1g}	781.6	0.33(1)

The 275.1-cm^{-1} mode curves slightly downwards whereas the 497.1 cm^{-1} bends slightly upwards.

B. X-ray diffraction

At ambient pressure (phase I), $CuAs_2O_4$ crystallizes in a tetragonal structure with space group $P4_2/mbc$ (no. 135) (see Fig. 1). The system contains Cu^{2+} spin chains running along the crystallographic c axis within CuO_2 ribbon chains. The ribbon chains are formed from linked basal planes of edge sharing CuO_6 octahedra. The CuO_6 octahedra experience Jahn-Teller distortions and are axially elongated along the crystallographic diagonals in the a-b plane. The octahedra are composed of two different oxygen sites, four O(2) atoms in the basal planes, and two O(1) atoms at the apex positions. The Cu–O(1) distances are enlarged by 20% compared to the Cu–O(2) distances reflecting strong Jahn-Teller distortions. The ribbon chains are twisted so that each edge of the CuO_2 ribbon chain has the buckled O(2)–O(2)–O(2) buckling angle of ∼168.2°, and the two edges have opposite senses of a buckling. The apex oxygen atoms are exactly centered above and below the Cu atoms such that the O(1)–Cu–O(1) angle amounts to 180°.

The reduction of the lattice parameters with pressure as determined from the x-ray-diffraction data is displayed in Fig. 4. The lattice compression is prominent along the a and b axes and less so along the c axis. Application of pressure leads to a nonlinear decrease in the distances between the Cu and the apex O(1) atoms. At 9 GPa, the decrease amounts to ∼10%. Consequently, the large reduction with pressure of the Cu–O(1) bond length implies a suppression of the Jahn-Teller elongation. The Cu–O(2) distances in the basal planes, however, decrease linearly with pressure and at 9 GPa the reduction amounts to only ∼1%. We have additionally plotted in Fig. 5 the Cu–O(2)–Cu angle, relevant for the NN super exchange, and the O(2)–O(2)–O(2) buckling angle. The Cu–O(2)–Cu angle decreases linearly with pressure and at 9 GPa the decrease amounts to ∼2.5%. The O(2)–O(2)–O(2) buckling angle decreases by ∼3.5% at 9 GPa.

Our x-ray-diffraction data evidence no symmetry change of the crystal structure up to a pressure of 9.2(2) GPa. At this pressure, we observe a structural phase transition from single-crystal phase I to single-crystal phase II. Figure 6 displays two single-crystal x-ray-diffraction frames for phase I and phase II with hkl indices of the Bragg reflections given. In phase II, the structure can be described by the space group $P\bar{4}2_1c$ (no. 114). The number of accessible Raman modes for $CuAs_2O_4$ in phase II is 52 compared to the 26 Raman modes accessible in phase

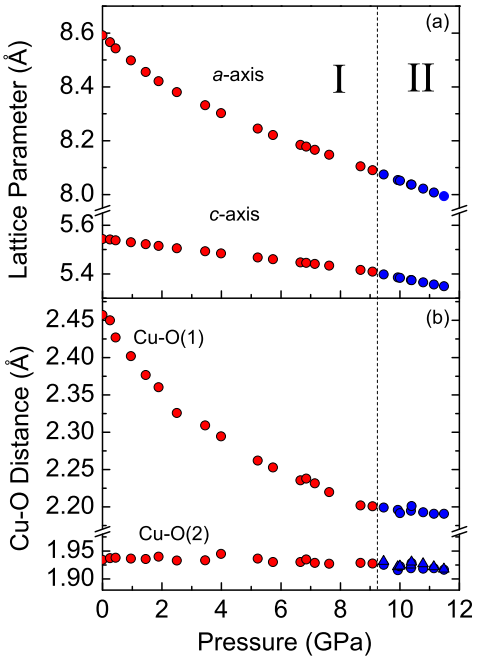

FIG. 4. (a) The lattice parameters of $CuAs_2O_4$ vs pressure in phase I and phase II. (b) The bond length of the Cu atoms to the apex oxygen atoms, Cu–O(1), and to the oxygen atoms in the equatorial plane [O(2) atoms]. In phase II two different Cu–O(2) distances are found which are labeled by different symbols. The nonlinear decrease of the Cu–O(1) distance with increasing pressure is clearly visible. Data points from phase I (red) and phase II (blue) are shown with the phase transition indicated by a dashed line.

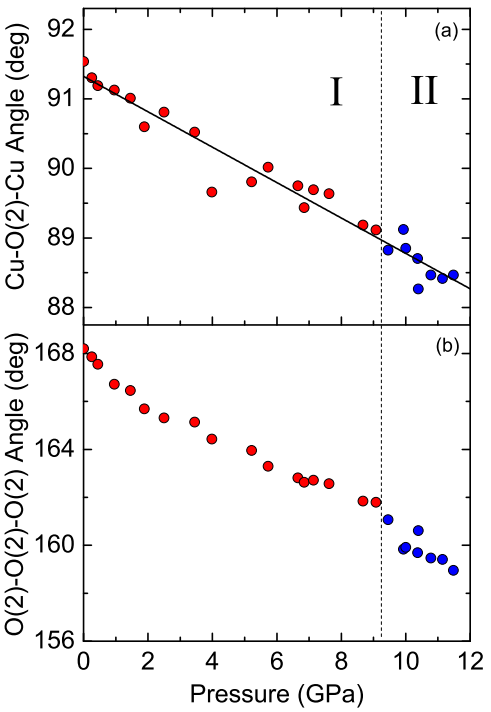

FIG. 5. The effect of pressure on the (a) NN exchange bonding angle, Cu–O(2)–Cu, and (b) the ribbon chain buckling angle, O(2)–O(2)–O(2). Data points from phase I (red) and phase II (blue) are shown with the phase transition indicated by a dashed line.

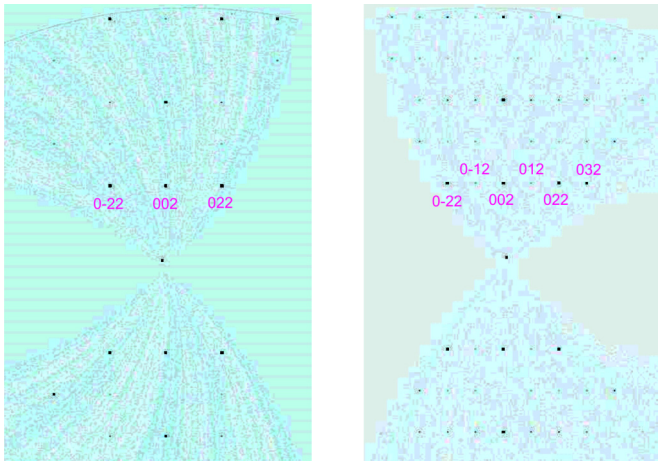

FIG. 6. Reciprocal space reconstruction of the $0kl$ plane of $CuAs_2O_4$ at 9.1 (phase I, left) and 10.4 GPa (phase II, right). Above 10.4 GPa, weak additional $0kl$ reflections with k odd appear.

I; we observed an increased number of modes in phase II. The structural parameters refined from the x-ray-diffraction data collected at ambient pressure and 11.5 GPa are summarized in Table II. A compilation of the structural parameters for all measured data at various pressures can be found in Ref. [47].

The transition from phase I to phase II is a *translationsgleiche* transition of index 2 according to $P4_2/mbc \rightarrow t2 \rightarrow P\bar{4}2_1c$, where $P\bar{4}2_1c$ is a maximal subgroup of $P4_2/mbc$. In phase II, $CuAs_2O_4$ maintains a tetragonal crystal structure supporting CuO_2 ribbon chains. Compared to phase I, the structural changes in phase II are predominantly found in the distortions of the oxygen octahedra. Figure 7 displays a projection of the CuO_6 octahedra chains along the [110] direction in the low- and high-pressure phases. In phase II, the four equidistant Cu–O(2) bonds in the basal plane split into two pairs with a distance difference of ~0.07% at 11.5 GPa. The O(2)–O(2)–O(2) buckling angle along the ribbon chains is significantly altered and amounts to 158.95° at 11.5 GPa

TABLE II. Structural parameters of phase I (0 GPa) and phase II (11.5 GPa) of $CuAs_2O_4$. The tabulated parameters for phase I were refined in space group $P4_2/mbc$ (no. 135) from the data obtained at ambient pressure with lattice parameters $a = 8.5913(11)$ Å and $c = 5.5437(1)$ Å. The tabulated parameters for phase II were refined from the data collected at 11.5 GPa assuming the space group $P\bar{4}2_1c$ (no. 114) with lattice parameters $a = 7.9945(1)$ Å and $c = 5.3491(1)$ Å.

	Atom:Wyck.	As:8*h*	Cu:4*d*	O(2):8*h*	O(1):8*g*
Phase I	Site symm.	*m*..	2.22	*m*..	..2
	x/*a*	0.16082	1/2	0.12221	0.20224
	y/*b*	0.20076	0	0.40137	0.70224
	z/*c*	0	1/4	0	1/4
	↓	↓	↓	↓	↓
	Atom:Wyck.	As:8*e*	Cu:4*d*	O(2):8*e*	O(1):8*e*
Phase II	Site symm.	1	2..	1	1
	x/*a*	0.31336	1/2	0.59751	0.28568
	y/*b*	0.33792	0	0.14146	0.16791
	z/*c*	0.23949	−0.02785	0.22233	0.01836

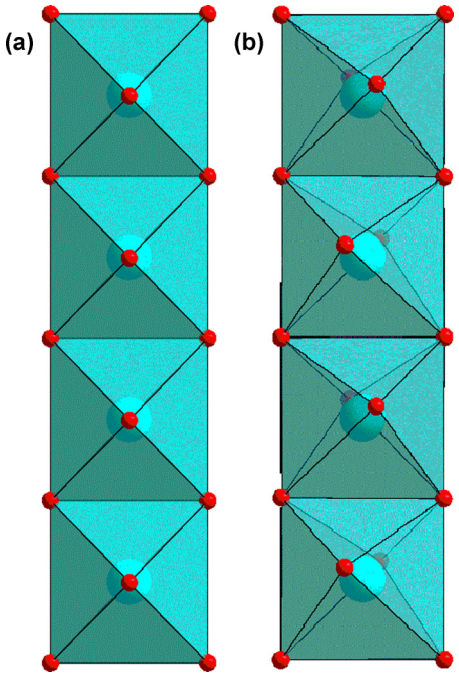

FIG. 7. Projection of the CuO_6 octahedra chains observed in phase I (a) and phase II (b) along [110]. The small (red) spheres represent O atoms and the larger (cyan) spheres represent Cu atoms. The deviation from 180° of the O(1)–Cu–O(1) angle formed by the apex oxygen atoms with the Cu atom can be clearly seen in phase II.

(Fig. 5). In phase II, the two As-O(1) bonds which are of equal length in phase I are split into two separate bonds differing by ~1%. Additionally, the apex O(1) atoms shift and they are no longer centered above and below the central Cu atoms. Consequently, in phase II the apex oxygen atoms form zig-zag chains along the *c* axis, above and below the CuO_4 basal planes [see Fig. 7(b)]. At 11.5 GPa, the O(1)–Cu–O(1) angle amounts to ~167° (increased twisting).

As shown in Fig. 8, there is a significantly larger decrease in the *a* and *b* axes with pressure as compared to the *c*-axis compression. The most noticeable effect of the large decrease in the *a* and *b* axes in phase I is the substantial reduction of the CuO_6 axial elongation. As seen in Fig. 8, up to ~7 GPa the decrease in the axial elongation with pressure is the main source of the compression of the base area, a^2, of the tetragonal cell. The relative change in the Cu–O(1) bond length with pressure coincides with twice the relative change in the lattice parameter *a*. The Cu–O(1) bond, being the weakest and most compressible bond in the CuO_6 octahedra, is therefore most significantly affected by a reduction of the cell volume. In the pressure regime of 0 to 7 GPa the Jahn-Teller elongation is strongly reduced whereas the Cu bonds to the equatorial O(2) atoms are hardly affected.

As the pressure is further increased above 7 GPa, the cell volume reduction is no longer controlled by a reduction of the Jahn-Teller elongation. Once this is sufficiently minimized, a structural phase transition occurs. The phase transition involves a loss of half of the symmetry elements and is most noticeable in the positions of the apex oxygen atoms O(1) and somewhat less of the oxygen atoms in the basal plane.

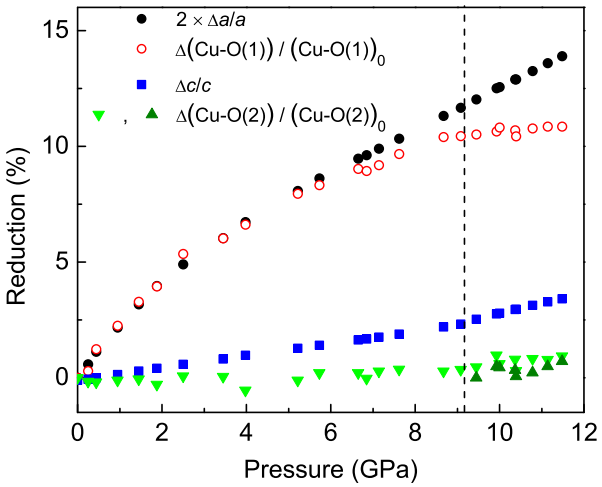

FIG. 8. Plot of the relative changes of various bond distances compared with the decrease of the lattice parameters.

In the structure representation Fig. 9, the displacement of the apex oxygen atoms is indicated by arrows. All atoms undergo a shift along the tetragonal c axis perpendicular to the a-b plane. Additionally, the apex oxygen atoms alternately tilt away from the tetragonal axis by a movement in the a-b plane. The buckling angle O(2)–O(2)–O(2), which measures the degree of twisting of the ribbon chains, reduces continuously with pressure (∼5% at 9 GPa) until the phase transition is reached [see Fig. 5(b)]. At the phase transition, a glitch is observed in the buckling angle and a further reduction is found in phase II. In contrast to the bucking angle, the NN bonding angle, Cu–O(2)–Cu, decreases continuously with pressure and shows no anomaly at the transition from phase I to phase II [see Fig. 5(a)].

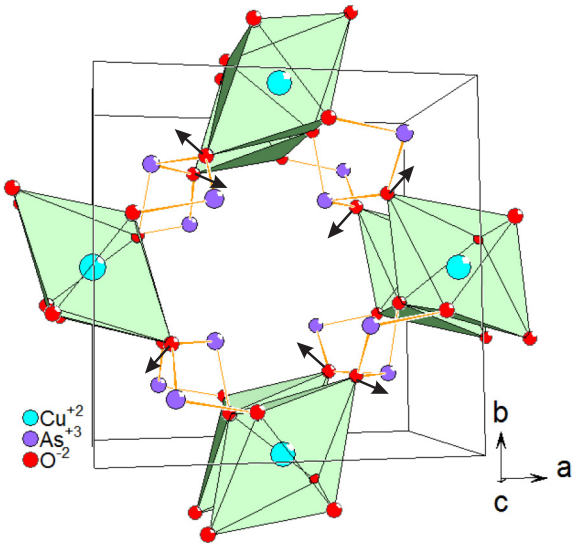

FIG. 9. $CuAs_2O_4$ structure at ambient pressure. Arrows represent the atom displacements initiated by the transition from phase I to phase II. The movement of all atoms along the c axis is significantly smaller than the displacement of the apex oxygen atom.

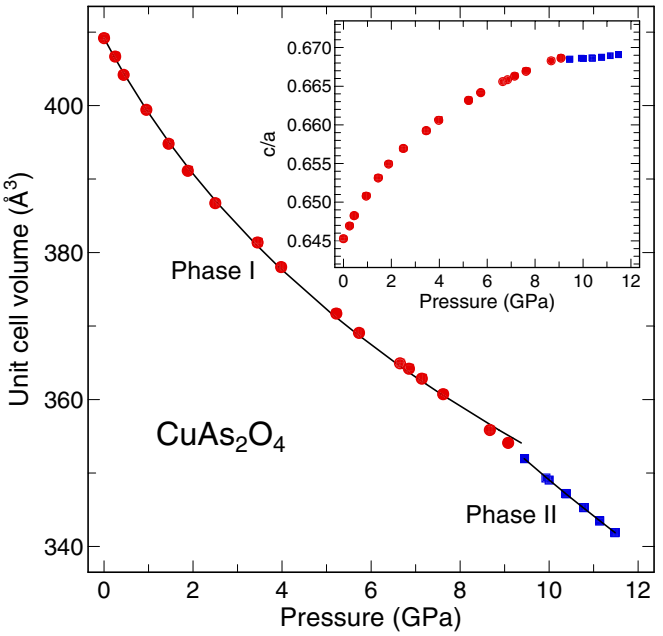

FIG. 10. $CuAs_2O_4$ unit-cell volume reduction with increasing external pressure. The inset displays the ratio of the lattice parameters c/a. The (red) points indicate the lattice parameters in phase I (space group $P4_2/mbc$) and the (blue) points indicate the parameters in phase II (space group $P\bar{4}2_1c$). The (black) solid lines represent the results of the fits to the Vinet equation of state with parameters listed in Table III.

Figure 10 presents the decrease in the unit-cell volume with pressure. The inset shows the c/a ratio of the tetragonal unit cell. With increasing pressure, the c/a ratio increases and saturates at the phase transition with a value of ∼0.67. In order to extract the bulk moduli and their derivatives with respect to pressure, the experimental pressure/volume relationships were fitted to a Vinet equation of state (EoS) [48]. The Vinet EoS can be expressed as

$$P = \frac{3\,K_{0,i}(1-x)}{x^2}\exp\left(\frac{3}{2}(K'_{0,i}-1)(1-x)\right), \qquad (2)$$

where $x = (V_i(P)/V_{0,i})^{1/3}$ with the volumes $V_{0,i}$ for the initial pressure for each phase (i = I, II), the bulk moduli $K_{0,i}$ and their derivatives at the initial pressure, $K'_{0,i}$. The fitted parameters are listed in Table III. In the phase II fit, $K'_{0,2}$ was fixed to a value of 4.

$CuAs_2O_4$ at ambient pressure conditions is isostructural to $FeSb_2O_4$ "Schafarzikite" [49]. In contrast to $CuAs_2O_4$, $FeSb_2O_4$ undergoes two subsequent structural phase

TABLE III. Parameters of the Vinet equation of state [Eq. (2)] fitted to the pressure/volume data of $CuAs_2O_4$. The derivative of the bulk moduli with respect to pressure, $K'_{0,2}$, was fixed to a value of 4 for phase II.

Phase	$V_{0,i}$ (Å^3)	$K_{0,i}$ (GPa)	$K'_{0,i}$
I (<9 GPa)	409.18(5)	36(2)	8.4(8)
II (>9 GPa)	351.92(9)	66(1)	4

transitions under pressure. From space group $P4_2/mbc$, $FeSb_2O_4$ transforms to $P2_1/c$ at ~4 GPa, followed by a transition to $P4_2/m$ at ~7 GPa [50]. In the $P4_2/mbc$ phase, the bulk modulus of $FeSb_2O_4$ amounts to 49(2) GPa, somewhat larger than what we find for $CuAs_2O_4$ in phase I. However, we find $CuAs_2O_4$ to follow an anisotropic compressibility with $K'_{0,1} = 8.4(8)$ for phase I. Values $K'_0 > 4$ are commonly found in nonisotropic structures. An analysis of the pressure induced atom displacements in the high-pressure phases of $FeSb_2O_4$ reveals very similar movements of the apex oxygen atoms, also forming a zig-zag chain at high pressure, and slight movements of the oxygen atoms in the basal planes. Below 43 K $FeSb_2O_4$ orders with a canted antiferromagnet structure and shows a concomitant magnetoelectric effect [51–54].

C. Evaluation of the spin-exchange constants

The structural changes with pressure in $CuAs_2O_4$ affect both the NN and NNN spin-exchange interactions. The NN exchange angle decreases from 91.5° at ambient pressure to 88.4° at 11.5 GPa as shown in Fig. 5. This angle decrease results from an increased twisting between two adjacent CuO_4 square planes, which enhances the FM component of the J_{nnn} by reducing the overlap between the O $2p$ orbitals (from the magnetic orbitals of the Cu^{2+} sites at the bridging O atoms) [55,56]. To determine the spin-exchange parameters for various pressures, we used *ab initio* calculations with the structural parameters determined from our x-ray-diffraction results. We followed the same method as employed in our previous investigation for ambient conditions [33]. We consider the NN intrachain exchange, J_{nn}, and the NNN intrachain exchange, J_{nnn}. The spin-exchange energies were evaluated by performing an energy-mapping analysis [55,56] based on first-principles DFT calculations for three ordered spin states (see Fig. 2 in Ref. [33]). The electronic energies of the three ordered spin states were calculated using the projected augmented-wave method [57,58] encoded in the Vienna *ab initio* simulation package (VASP) [59] and the generalized gradient approximation (GGA) for the exchange and correlation functional [60]. A set of 18 k points for the irreducible Brillouin zone was taken into account and the plane-wave cutoff energy was set to 400 eV. The effect of electronic correlations associated with the Cu $3d$ states was monitored by adding a variable on-site repulsion into the DFT calculations (DFT+U_{eff} calculations) with $U_{eff} = U - J$ ranging from 0 to 8 eV [61]. The energies of the ordered states were written in terms of the Heisenberg spin Hamiltonian:

$$\mathcal{H} = -\sum J_{ij}\vec{S}_i\vec{S}_j, \tag{3}$$

where the J_{ij}'s represent the exchange parameters for the coupling between spin sites i and j. According to the energy expressions for spin dimers with N ($N = 1$ in this case) unpaired spins per spin site [62,63], the total spin-exchange energies of the three ordered spin states, per eight formula units, are summarized in Table IV. Using J_{nn} and J_{nnn}, the Curie-Weiss temperatures, Θ_{CW}, listed in Table IV were calculated according to

$$\Theta_{CW} = \frac{1}{3}S(S+1)\sum_i z_i J_i. \tag{4}$$

TABLE IV. Values of J_{nn} and J_{nnn} obtained from the DFT + U_{eff} calculations. The structural parameters at ambient pressure (phase I) and at 11.48 GPa (phase II), given in Table II, were used for the calculations. The Curie-Weiss temperatures obtained using Eq. (4) are listed in the rightmost column. (Note that in Ref. [33], the previously reported spin-exchange constants at ambient pressure were erroneously scaled by a factor of 1/4.)

	U_{eff} (eV)	J_{nn} (K)	J_{nnn} (K)	Θ_{CW} (K)
Phase I	0	174.4	−100.7	36.9
	4	154.5	−52.9	50.8
	6	134.8	−39.0	47.9
	8	108.7	−27.5	40.6
Phase II	0	591.2	−80.5	235.4
	4	309.5	−57.3	126.1
	6	238.7	−43.6	97.6
	8	174.1	−31.2	71.5

For Cu^{2+}, a value $U_{eff} \sim 6$ to 8 eV is most appropriate [10,61]. Figure 11 shows the J_{nn} and J_{nnn} values (U_{eff} = 8 eV) plotted against pressure. In phase I, J_{nn} (ferromagnetic) increases with pressure by about 40% whereas J_{nnn} (antiferromagnetic) remains approximately constant.

Above 9.2 GPa in phase II, the increase of J_{nn} with pressure slows down whereas J_{nnn} becomes slightly more negative. As a consequence, the ratio $\alpha = J_{nn}/J_{nnn}$ (see Fig. 11 inset) passes through a shallow minimum and increases again in phase II.

We performed additional DFT+U_{eff} calculations to estimate the interchain spin-exchange interactions, J_{inter}, as a function of pressure. The two ordered spin states shown in Fig. 12 were used in the energy-mapping analysis assuming a global interchain exchange parameter between the Cu moments in neighboring chains [55,56]. The calculated

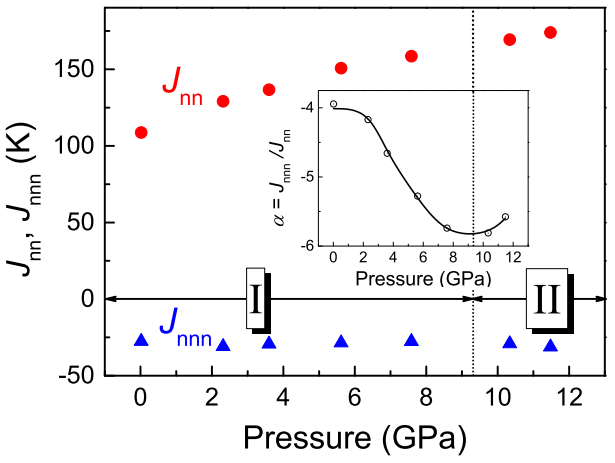

FIG. 11. Summary of the DFT+U_{eff} calculations depicting how the NN and NNN spin-exchange constants, J_{nn} and J_{nnn} (U_{eff} = 8 eV), and the ratio $\alpha = J_{nn}/J_{nnn}$ (inset), evolve with pressure in phase I and II.

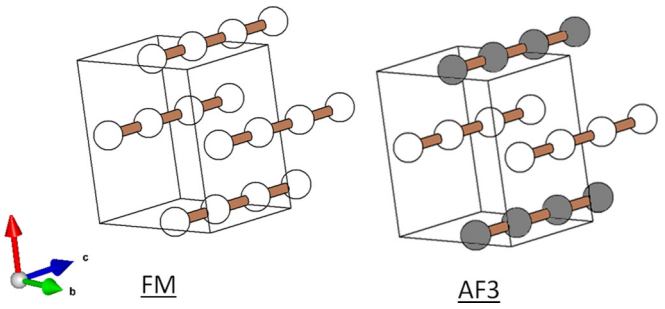

FIG. 12. Ordered spin states used for the DFT+U_{eff} calculations of the interchain spin-exchange interaction J_{inter}. The unfilled and filled atoms represent up and down spins, respectively.

interchain interactions are listed in Table IV. We find that at ambient pressure the interchain interactions are two orders of magnitude smaller than J_{nn} and at 11.48 GPa the interchain interactions are one order of magnitude smaller than J_{nn} and J_{nnn}.

D. Magnetic properties

Magnetization measurements as a function of pressure were performed to gain insight on how the structural changes and phase transition affect the magnetic properties of $CuAs_2O_4$. Figure 13 displays the magnetic ordering temperature, T_C, of $CuAs_2O_4$ versus pressure. In phase I, a stabilization of the FM ground state is indicated by an increase of T_C up to ~12 K. This is consistent with the increase of J_{nn} with pressure in phase I predicted by the DFT calculations. In phase II, we find that T_C drops to a value of ~7 K indicating an alteration of the magnetic properties. Up to the phase transition ($P <$ 9.2 GPa) ferromagnetic ordering is observed. The details of the long-range ordered state in phase II are difficult to ascertain due to the large background signal from the diamond anvil cell.

Although $CuAs_2O_4$ is primarily quasi-one-dimensional, the ground-state ordering results from both intrachain and interchain interactions, the competing intrachain interactions being the dominant spin-exchange interactions. As seen in Fig. 13, there is correlated behavior between the measured

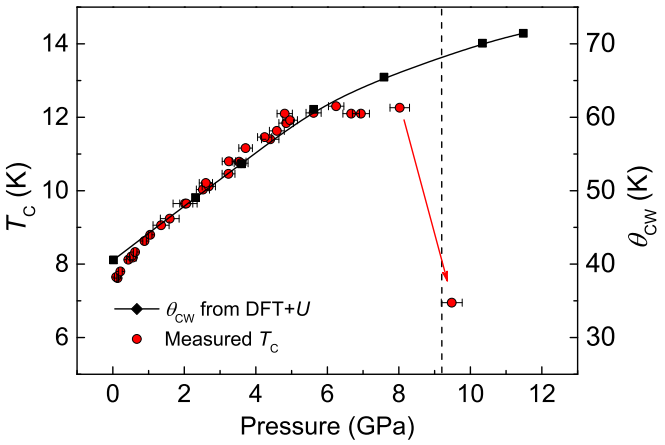

FIG. 13. Magnetic ordering temperature of $CuAs_2O_4$ vs pressure. We have added data taken from Ref. [33] for pressures below 1.5 GPa.

TABLE V. Values of the interchain spin-exchange interaction, J_{inter}, for various pressures obtained from DFT+U_{eff} calculations. The structural parameters obtained from synchrotron x-ray diffraction were used as input for the calculations with the ordered spin states shown in Fig. 12.

Pressure (GPa)	U_{eff} (eV)	J_{inter} (K)
0	0	5.8
	2	5.1
	4	2.7
	6	1.5
	8	0.9
7.62	0	34.0
	2	12.6
	4	5.8
	6	3.0
	8	1.7
10.00	0	36.6
	2	13.3
	4	6.0
	6	3.1
	8	1.7
11.48	0	33.9
	2	12.6
	4	8.8
	6	3.0
	8	1.6

T_C and calculated θ_{CW} values up to the pressure where the structural phase transition occurs. However, at the transition to phase II, T_c drops to a value of ~7 K, close to the value observed at ambient conditions in phase I. There is no substantial change of the interchain interaction at the transition from phase I to phase II (see Table V); however, at the phase transition the ratio of the NN to NNN spin-exchange interaction passes through a minimum. The rapid decrease of the long-range ordering temperature must be ascribed to a large sensitivity of the ground state to subtle details of the intrachain spin-exchange interaction rather than to the interchain spin exchange.

In order to characterize the increase in T_C with unit-cell volume in phase I, we fitted a linear relationship to $\Delta T_C(P)$ versus $\Delta v(P)$ according to

$$\beta = -\frac{\delta \ln[T_C(P)]}{\delta \ln[v(P)]} \approx -\frac{v(0)}{T_C(0)} \frac{\Delta T_C(P)}{\Delta v(P)}. \quad (5)$$

From the fitted results, we find best agreement with $\beta =$ 6.18(6).

IV. SUMMARY

We have studied the effect of hydrostatic pressure on the structural and magnetic properties of the quasi-one-dimensional quantum-spin-chain ferromagnet, $CuAs_2O_4$. At ambient pressure, this system contains CuO_2 ribbon chains with dominating NN ferromagnetic spin-exchange interactions. The NNN spin-exchange interactions, through O . . . O . . . O contacts, are antiferromagnetic and smaller than the NN spin exchange by a factor of ~4.1 in magnitude.

Consequently, $CuAs_2O_4$ represents a rare example of a quantum spin-chain system with competing spin-exchange interactions, which is in proximity to the quantum critical limit at $J_{nn}/J_{nnn} = -4$. At this critical point, the ferromagnetic phase and helicoidal AFM phase meet in the ground-state phase diagram [29]. We believe $CuAs_2O_4$ represents the first spin-chain system for which a FM ground state has been realized. Similar systems with ferromagnetically aligned chains, so far, have been found to order with an AFM ground state due to interchain interactions.

With the application of hydrostatic pressure, we have found a large suppression of the axial Jahn-Teller elongations of the oxygen octahedra surrounding the Cu^{2+} cations. We have also identified a structural phase transition leading to a new ribbon chain structure accompanied by a severe alteration of the magnetic properties. Before the phase transition, a stabilization of the FM ground state was indicated by a continuous increase of the magnetic ordering temperature. The phase transition induced a notable change of the magnetic properties which was signaled by a dramatic drop in the ordering temperature. Using DFT calculations, we have shown that hydrostatic pressure decreases $\alpha = J_{nn}/J_{nnn}$ from ~ -4 at ambient pressure to ~ -6 at 11.5 GPa with a minimum at the phase transition and a slight growth in phase II. The drop of the long-range ordering signals a high sensitivity of the ground state to subtle details of the dominant intrachain spin-exchange interactions.

In conclusion, our investigations demonstrate that it is possible to reach new magnetic ground states in ribbon chain systems through the application of external pressure. Similar investigations could be carried out on other ribbon chain compounds and may lead to the realization of unique magnetic ground states such as helical ordering and possibly multiferroicity.

ACKNOWLEDGMENTS

We are grateful to S. Höhn, E. Brücher, G. Siegle, and S.-M. Souliou for expert experimental assistance. M.H.W. thanks the Natural Energy Research Scientific Computing Center and the High-Performance Computing Center of North Carolina State University for the computing resources. We thank F. Pertlik for providing the samples.

[1] B. J. Gibson, R. K. Kremer, A. V. Prokofiev, W. Assmus, and G. J. McIntyre, Physica B **350**, e253 (2004).
[2] T. Masuda, A. Zheludev, A. Bush, M. Markina, and A. Vasiliev, Phys. Rev. Lett. **92**, 177201 (2004).
[3] M. Enderle, C. Mukherjee, B. Fåk, R. K. Kremer, J.-M. Broto, H. Rosner, S.-L. Drechsler, J. Richter, J. Malek, A. Prokofiev, W. Assmus, S. Pujol, J.-L. Raggazzoni, H. Rakoto, M. Rheinstädter, and H. M. Rønnow, Europhys. Lett. **70**, 237 (2005).
[4] S.-L. Drechsler, J. Richter, R. Kuzian, J. Málek, N. Tristan, B. Büchner, A. S. Moskvine, A. A. Gippius, A. Vasiliev, O. Volkova, A. Prokofiev, H. Rakoto, J.-M. Broto, W. Schnelle, M. Schmitt, A. Ormeci, C. Loison, and H. Rosner, J. Mag. Mag. Mater. **316**, 306 (2007).
[5] S.-L. Drechsler, O. Volkova, A. N. Vasiliev, N. Tristan, J. Richter, M. Schmitt, H. Rosner, J. Málek, R. Klingeler, A. A. Zvyagin, and B. Büchner, Phys. Rev. Lett. **98**, 077202 (2007).
[6] J. Sirker, Phys. Rev. B **81**, 014419 (2010).
[7] B. Willenberg, M. Schäpers, K. C. Rule, S. Süllow, M. Reehuis, H. Ryll, B. Klemke, K. Kiefer, W. Schottenhamel, B. Büchner, B. Ouladdiaf, M. Uhlarz, R. Beyer, J. Wosnitza, and A. U. B. Wolter, Phys. Rev. Lett. **108**, 117202 (2012).
[8] S. Park, Y. J. Choi, C. L. Zhang, and S-W. Cheong, Phys. Rev. Lett. **98**, 057601 (2007).
[9] Y. Naito, K. Sato, Y. Yasui, Y. Kobayashi, and M. Sato, J. Phys. Soc. Jpn. **76**, 023708 (2007).
[10] H. J. Xiang and M.-H. Whangbo, Phys. Rev. Lett. **99**, 257203 (2007).
[11] Y. Mizuno, T. Tohyama, S. Maekawa, T. Osafune, N. Motoyama, H. Eisaki, and S. Uchida, Phys. Rev. B **57**, 5326 (1998).
[12] Y. Yasui, Y. Naito, K. Sato, T. Moyoshi, M. Sato, and K. Kaurai, J. Phys. Soc. Jpn. **77**, 023712 (2008).
[13] F. Schrettle, S. Krohns, P. Lunkenheimer, J. Hemberger, N. Büttgen, H.-A. Krug von Nidda, A. V. Prokofiev, and A. Loidl, Phys. Rev. B **77**, 144101 (2008).
[14] A. S. Moskvin and S.-L. Drechsler, Europhys. Lett. **81**, 57004 (2008).
[15] Y. Matiks, P. Horsch, R. K. Kremer, B. Keimer, and A. V. Boris, Phys. Rev. Lett. **103**, 187401 (2009).
[16] A. Ruff, S. Krohns, P. Lunkenheimer, A. Prokofiev, and A. Loidl, J. Phys. Condens. Matter **26**, 485901 (2014).
[17] M. Mourigal, M. Enderle, R. K. Kremer, J. M. Law, and B. Fåk, Phys. Rev. B **83**, 100409(R) (2011).
[18] M. Mourigal, M. Enderle, B. Fåk, R. K. Kremer, J. M. Law, A. Schneidewind, A. Hiess, and A. Prokofiev, Phys. Rev. Lett. **109**, 027203 (2012).
[19] L. Capogna, M. Mayr, P. Horsch, M. Raichle, R. K. Kremer, M. Sofin, A. Maljuk, M. Jansen, and B. Keimer, Phys. Rev. B **71**, 140402(R) (2005).
[20] L. Capogna, M. Reehuis, A. Maljuk, R. K. Kremer, B. Ouladdiaf, M. Jansen, and B. Keimer, Phys. Rev. B **82**, 014407 (2010).
[21] A. U. B. Wolter, F. Lipps, M. Schäpers, S.-L. Drechsler, S. Nishimoto, R. Vogel, V. Kataev, B. Büchner, H. Rosner, M. Schmitt, M. Uhlarz, Y. Skourski, J. Wosnitza, S. Süllow, and K. C. Rule, Phys. Rev. B **85**, 014407 (2012).
[22] S.-L. Drechsler, N. Tristan, R. Klingeler, B. Büchner, J. Richter, J. Málek, O. Volkova, A. Vasiliev, M. Schmitt, A. Ormeci, C. Loison, W. Schnelle, and H. Rosner, J. Phys. Condens. Matter **19**, 145230 (2007).
[23] M. G. Banks, R. K. Kremer, C. Hoch, A. Simon, B. Ouladdiaf, J.-M. Broto, H. Rakoto, C. Lee, and M.-H. Whangbo, Phys. Rev. B **80**, 024404 (2009).
[24] C. Lee, Jia Liu, M.-H. Whangbo, H.-J. Koo, R. K. Kremer, and A. Simon, Phys. Rev. B **86**, 060407(R) (2012).
[25] S. Seki, T. Kurumaji, S. Ishiwata, H. Matsui, H. Murakawa, Y. Tokunaga, Y. Kaneko, and T. Hasegawa, and Y. Tokura, Phys. Rev. B **82**, 064424 (2010).

[26] L. Zhao, T.-L. Hung, C.-C. Li, Y.-Y. Chen, M.-K. Wu, R. K. Kremer, M. G. Banks, A. Simon, M.-H. Whangbo, C. Lee, J. S. Kim, I. Kim, and K. H. Kim, Adv. Mater. **24**, 2469 (2012).
[27] J. Liu, H.-J. Koo, H. Xiang, R. K. Kremer, and M.-H. Whangbo, J. Chem. Phys. **141**, 124113 (2014).
[28] T. Hikihara, M. Kaburagi, and H. Kawamura, Phys. Rev. B **63**, 174430 (2001).
[29] S. Furukawa, M. Sato, and S. Onoda, Phys. Rev. Lett. **105**, 257205 (2010).
[30] M. Schmitt, J. Málek, S.-L. Drechsler, and H. Rosner, Phys. Rev. B **80**, 205111 (2009).
[31] R. O. Kuzian, S. Nishimoto, S.-L. Drechsler, J. Málek, S. Johnston, J. van den Brink, M. Schmitt, H. Rosner, M. Matsuda, K. Oka, H. Yamaguchi, and T. Ito, Phys. Rev. Lett. **109**, 117207 (2012).
[32] M. Matsuda, K. Ohoyama, and M. Ohashi, J. Phys. Soc. Jpn. **68**, 269 (1999).
[33] K. Caslin, R. K. Kremer, F. S. Razavi, A. Schulz, A. Muñoz, F. Pertlik, J. Liu, M.-H. Whangbo, and J. M. Law, Phys. Rev. B **89**, 014412 (2014).
[34] K. Caslin, Ph.D. thesis, Brock University, 2015.
[35] F. Pertlik, Z. Anorg. Allg. Chem. **436**, 201 (1977).
[36] K. Syassen, High Press. Res. **28**, 75 (2008).
[37] M. Merlini and M. Hanfland, High Press. Res. **33**, 511 (2013).
[38] H. K. Mao, J. Xu, and P. M. Bell, J. Geophys. Res. **91**, 4673 (1986).
[39] Oxford Diffraction: Data collection and data reduction GUI, CrysAlis Pro, ver. 171.34.44, Oxford Diffraction Ltd., 2010.
[40] cf. http://wwwba.ic.cnr.it/content/sir2011-v10.
[41] cf. http://www.xtl.ox.ac.uk/crystals.html.
[42] V. Petricek, M. Dusek, and L. Palatinus, Z. Kristallogr. **229**, 345 (2014).
[43] N. Tateiwa, Y. Haga, Z. Fisk, and Y. Onuki, Rev. Sci. Instr. **82**, 053906 (2011).
[44] N. Tateiwa, Y. Haga, T. D. Matsuda, and Z. Fisk, Rev. Sci. Instr. **83**, 053906 (2012).
[45] A. Eiling and J. S. Schilling, J. Phys. F **11**, 623 (1981).
[46] R. Lortz (private communication).
[47] See Supplemental Material at http://link.aps.org/supplemental/10.1103/PhysRevB.93.022301 for a complete list of structural parameters for all measured pressures.
[48] P. Vinet, J. R. Smith, J. Ferrante, and J. H. Rose, Phys. Rev. B **35**, 1945 (1987).
[49] R. Fischer and F. Pertlik, Tscher. Miner. Petrog. **22**, 236 (1975).
[50] B. Hinrichsen, R. E. Dinnebier, P. Rajiv, M. Hanfland, A. Grzechnik, and M. Jansen, J. Phys. Condens. Matter **18**, S1021 (2007).
[51] J. A. Gonzalo, D. E. Cox, and G. Shirane, Phys. Rev. **147**, 415 (1966).
[52] R. Charter, J. R. Gavarri, and A. Hewat, J. Solid State Chem. **60**, 78 (1985).
[53] G. Gorodetsky, M. Sayar, and S. Shtrikman, Mat. Res. Bull. **5**, 253 (1970).
[54] A. Iyama, Y. Wakabayashi, N. Hanasaki, and T. Kimura, Jpn. J. Appl. Phys. **53**, 05FB02 (2014).
[55] M. Whangbo, H. Koo, and D. Dai, J. Solid State Chem. **176**, 417 (2003).
[56] H. J. Xiang, C. Lee, H.-J. Koo, X. G. Gong, and M.-H. Whangbo, Dalton Trans. **42**, 823 (2013).
[57] P. E. Blöchl, Phys. Rev. B **50**, 17953 (1994).
[58] G. Kresse and D. Joubert, Phys. Rev. B **59**, 1758 (1999).
[59] G. Kresse and J. Furthmüller, Phys. Rev. B **54**, 11169 (1996).
[60] J. P. Perdew, A. Ruzsinszky, G. I. Csonka, O. A. Vydrov, G. E. Scuseria, L. A. Constantin, X. Zhou, and K. Burke, Phys. Rev. Lett. **100**, 136406 (2008).
[61] S. L. Dudarev, G. A. Botton, S. Y. Savrasov, C. J. Humphreys, and A. P. Sutton, Phys. Rev. B **57**, 1505 (1998).
[62] D. Dai and M. Whangbo, J. Chem. Phys. **114**, 2887 (2001).
[63] D. Dai and M. Whangbo, J. Chem. Phys. **118**, 29 (2003).